Journal of Electric Propulsion

RESEARCH Open Access

Effects of a magnetic discontinuity in a modified Advanced Cusp Field Thruster

Leonard Bauer[1,2*], Max Vaupel[1], Hans Blättermann[1], Franz Georg Hey[1] and Peter J. Klar[2]

*Correspondence:
leonard.bauer@airbus.com

[1] Airbus Defence and Space GmbH, Claude-Dornier-Straße 1, 88090 Immenstaad, Germany
[2] I. Physikalisches Institut, Justus Liebig University Giessen, Heinrich-Buff-Ring 16, 35392 Giessen, Germany

Abstract

Deviations from the ideal magnetic configuration in a modified Advanced Cusp Field Thruster (ACFT) without cylindrical symmetry are examined to understand their effect on electron behavior and thruster performance. Spatially resolved measurements of the magnetic field (B-field) and temperature at the central magnetic cusp during operation are compared with full-sized 3D particle-tracing simulations of electrons. The simulations reveal that, in addition to the well-known $E \times B$ drift, electrons also undergo circumferential motion due to magnetic field gradients and curvature, effects not previously associated with Cusp Field Thrusters (CFTs). Even small imperfections in the magnet configuration are found to measurably affect both the B-field and local heating at the thruster's pole shoes. These results demonstrate that local deviations from ideal magnetic symmetry reduce electron confinement, increase wall losses, and ultimately affect thruster efficiency.

Keywords: Cusp Field Thruster, Thermal, Magnetic, Simulation

Introduction

Electric propulsion systems have become essential for modern spacecrafts, offering more efficient propellant use than chemical thrusters. By utilizing electric fields to accelerate ions away from the spacecraft, the various electric thruster types primarily differ in the methods used for efficiently maintaining ion generation [1]. Among these, Hall Thrusters (HTs) extend electron paths between cathode and anode with a magnetic field without fully trapping electrons [2, 3]. Since the early 2000 s, the Cusp Field Thruster (CFT) concept has gained attention, highlighted by developments such as Thales' Highly Efficient Multistage Plasma Thruster [4] and MIT's Diverging Cusped-Field Hall Thruster [5]. First introduced in the 1960 s [6], the CFT relies on sets of magnetic cusps "magnetic bottles" to achieve strong electron confinement. Since 2009, Airbus, together with Justus Liebig University of Giessen, has been developing its own variant: The Advanced Cusp Field Thruster (ACFT) [7, 8], with performance and principles reported in previous work [9–13].

For CFTs, maximizing electron confinement is critical to ensure ionization efficiency. Insufficient confinement causes energetic electrons to be lost to the discharge channel or anode, increasing wall heating and sputtering. While simulations based on idealized

© The Author(s) 2026. **Open Access** This article is licensed under a Creative Commons Attribution 4.0 International License, which permits use, sharing, adaptation, distribution and reproduction in any medium or format, as long as you give appropriate credit to the original author(s) and the source, provide a link to the Creative Commons licence, and indicate if changes were made. The images or other third party material in this article are included in the article's Creative Commons licence, unless indicated otherwise in a credit line to the material. If material is not included in the article's Creative Commons licence and your intended use is not permitted by statutory regulation or exceeds the permitted use, you will need to obtain permission directly from the copyright holder. To view a copy of this licence, visit http://creativecommons.org/licenses/by/4.0/.

Springer

magnetic fields often predict high confinement, practical thrusters rely on permanent magnets whose manufacturing introduces small but significant field asymmetries [14, 15]. These deviations break the ideal symmetry of the magnetic mirror structure and can weaken electron confinement, affecting thruster performance. Most simulation studies use idealized, symmetric magnetic field configurations for computational efficiency [16–22]. As a result, they may overestimate confinement and underpredict localized wall losses, since real-world magnet imperfections are not represented.

This study investigates the effects of magnetic asymmetry in a linear ACFT, a design that deliberately breaks cylindrical symmetry. By combining B-field and temperature measurements with full-scale 3D particle-tracing simulations of unperturbed electrons in static electromagnetic fields, we directly connect observed magnetic deviations to changes in electron behavior and thruster performance. Additionally, the employed 3D particle-tracing analysis highlights three-dimensional phenomena associated with CFTs that have not been previously discussed.

The "Advanced cusp field thruster" section reviews the ACFT operating principle and electron dynamics, followed by the "Linear advanced cusp field thruster" section, which introduces the linear modification. The "Experiment" and "Simulation" sections describe our experimental approach and method, respectively. Finally, the "Results" section presents the discussion, and the "Conclusion" section concludes.

Advanced Cusp Field Thruster

The operating principle of a CFT is similar to that of a HT. In both systems, ions are produced and the plasma is sustained by electron bombardment of neutral gas propellant within a discharge vessel. The generated thrust results from accelerating these ions with an electric field at the exit of the thruster. In both devices, a high electric potential is applied at the anode upstream inside the thruster, but due to the dense plasma in the discharge channel, the potential is effectively shielded up to the exit, where the plasma density decreases and the electric potential drops [16, 22].

A key difference between HTs and CFTs is in the confinement of electrons within the discharge chamber. Both designs aim to minimize energy loss while sustaining the plasma discharge. HTs use a magnetic field perpendicular to the electric field to extend electron paths, but do not fully trap them. In contrast, CFTs use a configuration of magnetic mirrors that fully trap electrons inside the discharge channel. The ions, due to their larger mass, are less affected by the magnetic field and can move freely toward the exit, where they are accelerated by the drop of the electric potential [8, 16]. Electron behavior is thus crucial to overall efficiency, as electrons that escape without ionizing the propellant reduce both propellant and power efficiency per unit thrust.

The Lorentz force causes electrons to gyrate around the B-field lines, converting perpendicular momentum into a spiral motion. In addition, electrons exhibit a net movement parallel to the field, the so-called guiding center motion. Magnetic cusps act as mirrors, reflecting electrons and trapping them in a "magnetic bottle", significantly extending their residence time in the discharge channel. This increased confinement allows electrons to undergo multiple collisions with neutral gas atoms, maintaining ionization even though the mean free path of electrons can be much longer than the discharge channel itself [16].

Electrons are reflected at a magnetic mirror if their energy meets the mirror condition, reversing the direction of their guiding center and sending them toward the next cusp, which again acts as a mirror [6, 8]. Once trapped between two such mirrors, an electron remains confined until it interacts with another plasma particle. The condition for confinement is determined by the electron's velocity vector and the B-field along its trajectory [23]:

$$\frac{B_0}{B_{\max}} = \frac{v_{0,\perp}^2}{v_{\max,\perp}^2} = \frac{v_{0,\perp}^2}{v_0^2}. \tag{1}$$

Here, B_0 is the B-field at the electron's origin, $B_{\max}$ is the field at the reflection point, $v_{0,\perp}$ is the initial velocity perpendicular to the field, and v_0 the total initial velocity. At the reflection point, the parallel velocity vanishes, so $v_0 = v_{\max,\perp}$.

The ACFT uses two permanent magnets which are oriented in such a way that both magnetic south poles meet in the same spatial region where a steel pole shoe is inserted. The resulting B-field near these opposing poles exhibits high gradients and small curvature radii. Similar magnetic cusps form at the anode and at the thruster exit (see Fig. 1). The anode, which also serves as the gas inlet, is made of ferromagnetic material and acts as the effective north pole of the upstream magnet.

An electron approaching or leaving a mirror moves primarily in the X-Y plane, radially outward from the thruster's symmetry axis and toward the discharge chamber wall. After reflection, the guiding center follows the B-field curvature, moving parallel to the symmetry axis (along Z), thus traversing the discharge chamber. The electron's guiding

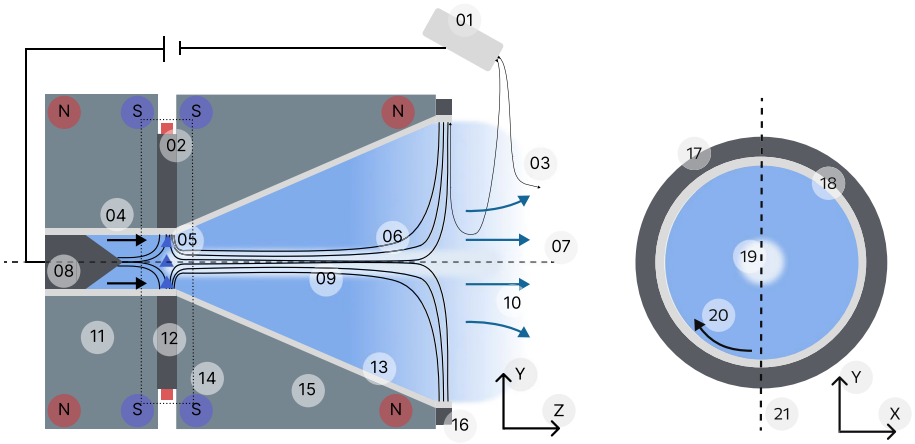


Fig. 1 Left: Cut view of an ACFT in the Z-Y plane, with the cut location indicated by (21). The numbers denote: neutralizer cathode (1), welded thermocouple locations (red squares, 2), beam path of neutralizing electrons (3), neutral gas feed (4), Hall probe locations (blue triangles, 5), B-field lines and trapped electron paths (6), symmetry axis (7), anode (8), central plasma region (9), accelerated ions (10), back magnet (11), center pole shoe (12), discharge chamber (13), region of interest for Fig. 2 (14), front magnet (15), and front pole shoe (16). The permanent magnets' magnetization is along Z, direction determined by N/S markings. Right: X-Y cut of cylindrical ACFT, with: center pole shoe (17), discharge chamber wall (18), central plasma region (19), circumferential drift (20), and symmetry axis (21). The magnets, with the ferromagnetic anode and pole shoes, focus B-field lines into cusps, extending electron residence time for ionization. The applied voltage between anode and cathode is typically 300–1200,V. Pole shoes are made of steel to allow direct thermocouple welding

center therefore oscillates back and forth through the channel, primarily parallel to the symmetry axis (denoted as (7) in Fig. 1).

Without additional drift effects, the electron's guiding center would stay within the X-Z plane, following a single B-field line as indicated by (6) in Fig. 1. However, the guiding center also drifts perpendicular to the B-field lines, producing a circumferential motion, known as "closed drift orbit" or "azimuthal drift" (indicated by (20) in Fig. 1).

Previous studies have not explained this motion or have attributed it solely to the $E \times B$ drift [17, 18, 21]. Ref. [24] demonstrates that the drift motion predominantly occurs near the exit, where the electric potential gradient becomes significant [16, 25]. Ref. [20] states the need for a 3D simulation to fully resolve the azimuthal drift. This velocity contribution due to drift results in an additional movement of the guiding center along the circumferential direction, as indicated by (12) in Fig. 2. It is given by [23]:

$$\vec{v}_{E\times B} = \frac{\vec{E} \times \vec{B}}{B^2}, \tag{2}$$

where $\vec{E}$ is the electric field vector and $\vec{B}$ is the B-field vector. The drift behavior of the electrons' guiding center is well understood and can be analytically described using the Lorentz force, which governs the motion of a single particle in electromagnetic fields [23]. While a gradient parallel to the B-field lines and the motion of the guiding center leads to the repelling force of the magnetic mirror, a gradient perpendicular to the

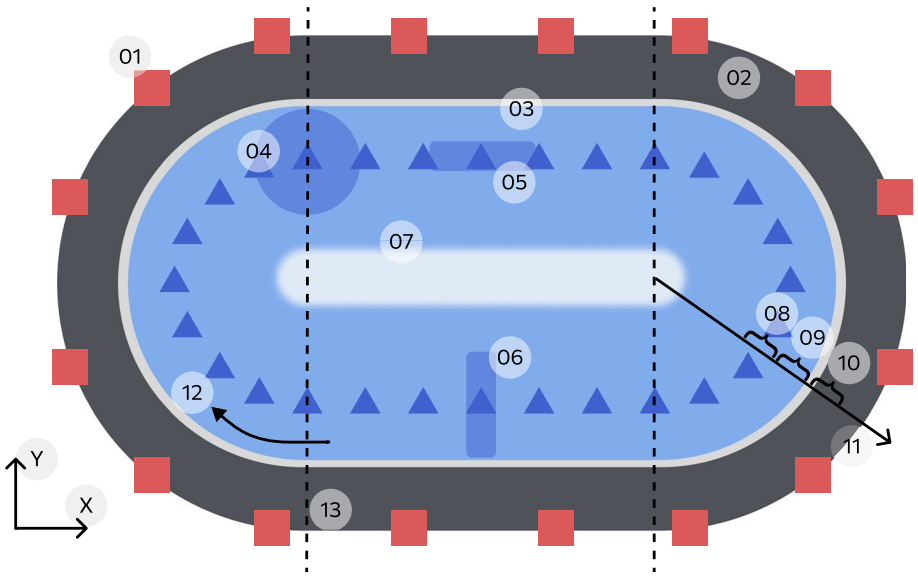


Fig. 2 Schematic view of the cross section perpendicular to the symmetry axis of the linear ACFT at the center pole shoe as highlighted in Fig. 1 (14): Locations of the welded thermocouples on the outside are presented as red squares and denoted by (1), center pole shoe (2), discharge chamber (3), physical dimensions of the axial Hall probe and the measurement locations as blue triangles (4), dimensions of the radial Hall probe in the two used orientations (5) and (6), central plasma region (7), radial distance of the B-field measurements (8), radial distance of the magnetic mirror (9), radial distance of electron impacts (10), radial direction vector (11), circumferential/drift direction vector (12) and reduction of full cylindrical symmetry (13). Due to physical dimensions of the Hall probe, the B-field measurements are not performed directly at the magnetic cusps but only at the locations marked with a triangle. Every position was measured with both radial probes (5) and (6) as well as the axial probe (4)

B-field lines leads to an out of plane drifting motion, adds to the $E \times B$ drift. This velocity component of the electrons' drift is called the "gradient drift", and is given by [23]:

$$\vec{v}_{\text{Grad}} = \frac{1}{2} v_{\perp} r_L \frac{\vec{B} \times \nabla B}{|B|^2}. \tag{3}$$

Here, $\vec{v}_{\text{Grad}}$ is the drift velocity due to the gradient drift, $v_{\perp}$ is the velocity component of the electron relative to the local B-field $\vec{B}$ and r_L is the Larmor radius of the electron. The third velocity component of the drifting motion stems from the curvature of the B-field. Its direction also adds to the $E \times B$ drift, and this curvature drift is given by:

$$\vec{v}_{\text{Curv}} = \frac{m v_{\parallel}^2}{q|B|^2} \frac{\vec{R_C} \times \vec{B}}{\vec{R_C}^2}. \tag{4}$$

Here, m is the mass and q is the charge of the electron, $v_{\parallel}$ is the velocity component parallel to the local B-field $\vec{B}$, and $\vec{R_C}$ is the local curvature radius of the B-field [23].

Therefore, in addition to axial and radial movement in the Z-X plane shown in Fig. 1, the combined effects of the curvature and gradient of the magnetic field, as well as the gradient of the electric potential, lead to motion out of the Z-X plane. This direction is indicated by (20) in Fig. 1 and (12) in Fig. 2. The combined motion of the electrons, gyration around the B-field lines between the mirrors, and the various drift motions, is shown in Fig. 4 in "Simulation" section and is discussed in "Simulation" and "Results" sections.

If the magnets of a cylindrical ACFT are perfectly symmetric and aligned, single electron behavior, specifically confinement and electron drifting remains uniform around the circumference. Previous studies have therefore often used 2D simulations or idealized 3D models, and variations in electron behavior around the circumference have not been reported [16–20].

However, real magnets have manufacturing tolerances that introduce small variations in their properties [14, 15]. Physical deviations in geometry within these tolerances mean that operational cylindrical ACFTs show variations in mirror strength along the circumference. The same applies to the linear ACFT (see Fig. 2 and "Linear advanced cusp field thruster" section), which lacks full cylindrical symmetry.

If an electron's mean free path is long, it can drift from a region with strong confinement to one with weaker mirrors, passing through and being lost at the walls. However, looking at Eq. 3 it becomes clear that at least the velocity component due to the gradient drift depends on the magnitude of ∇B, which means that the drift inside a region where the B-field near the wall is weaker, is slower and the electrons thus reside even longer in these regions and need to make more successful reflections. Thus, even small local regions of weak magnetic mirrors can significantly impact performance, as they cause localized heating and disrupt the ionization cascade.

In this study, we use a full-scale 3D particle-tracing simulation to model unperturbed electron trajectories in static fields, quantifying circumferential drifting phenomena in a linear ACFT and assessing how magnet non-ideality or misalignment affects thruster performance. The choice of this approach over full PIC simulation, and its implications, are discussed in "Simulation" section.

Linear Advanced Cusp Field Thruster

To study the effects of magnetic anomalies and broken symmetry in cusp regions, we investigate a modified version of the ACFT that intentionally departs from cylindrical symmetry. This linear ACFT introduces additional straight segments into the cross-section, resulting in a racetrack-shaped geometry with a 180° rotational symmetry axis and two perpendicular mirror planes, instead of full cylindrical symmetry. Despite this change, the core schematic and physical principles illustrated in Fig. 1 remain applicable.

In contrast to variations in B-field strength along the circumference of cylindrical ACFTs caused by manufacturing tolerances, this symmetry reduction introduces an inherent inhomogeneity in the magnetic field along the circumference of a linear ACFT. Hence, the linear section deliberately introduces areas where the confinement of the electrons via the magnetic mirror is weakened. Thus, it is expected that the number of electrons passing through the mirror in these linear sections is increased. This leads to a non-negligible heating of the walls of the discharge chamber in those sections as the electrons' energy is deposited at the walls in the form of heat.

The movement of the electrons' guiding center remains primarily back and forth along the radial and axial directions of the B-field. The out-of-plane drifting also stays in the circumferential direction, which is no longer a circle, but two semi-circles with two linear sections in between as indicated by (12) in Fig. 2.

A previous performance characterization has shown that the linear ACFT is less efficient than its symmetric counterpart [12, 26]. Nevertheless, we use the same linear ACFT unit as in prior research in this study, allowing us to build on previous findings and deepen our understanding of the link between geometry, magnetic field variation, and electron losses in this configuration.

Experiment

This study's approach is evaluated through three complementary experimental methods. First, B-field inside the linear ACFT is measured under ambient conditions at multiple spatial locations. Second, temperature distribution along the central pole shoe is recorded during steady-state thruster operation in vacuum. Third, the plasma plume profile is mapped with high spatial resolution.

The B-field measurement allows us to assess the impact of manufacturing and assembling tolerances on the thruster's magnetic configuration and to correlate it with its performance. The B-field is measured with both axial and radial Hall probes attached to a HIRST Magnetic Instruments GM08. Measuring in the two radial orientations as well as in the axial orientation of the Hall probe, the local magnetic flux density vector $\vec{B}$ at each location is fully characterized. The measurement is performed as close to the wall as allowed by the dimensions of the probe, which is about 2.5 mm away from the inner surface of the actual pole shoe surface. Consequently, the B-field exactly at the magnetic mirror position (e.g., (9) in Fig. 2) cannot be measured. Using several additively manufactured guide pieces, B-field measurements were performed at 28 locations in the plane of the magnetic cusp. The probe positions are indicated by blue triangles in Figs. 1 and 2.

The measurement accuracy depends on the probe's positional uncertainty and its intrinsic measurement accuracy. The guide pieces and probes are friction-fitted, yielding

an estimated positional uncertainty of approximately 0.2 mm, determined by the 3D printer's precision. The probe accuracy is within 0.5% of the measured value. Each location was measured three times per probe orientation, with relative standard deviations of 3% to 7%.

The measured values at these positions can later be compared to the values of the simulation at these locations. If the measured and simulated B-fields agree at all accessible probe locations, we infer the simulations reliably represent regions inaccessible to the probes, such as the pole shoe surface. Figures 6 and 7 show magnetic field distributions at both accessible and inaccessible positions, alongside simulated electron impact density. The electron impacts around the pole shoe are also shown in Fig. 4. Figures 5 and 7 present temperature distributions measured on the pole shoe's exterior.

To measure this temperature distribution sixteen type K thermocouples are welded equidistantly around the pole shoe's outer circumference (see red squares (1) in Fig. 2 and (2) in Fig. 1). The steel pole shoe only contacts the magnets and the discharge chamber. Heat enters the pole shoe via the discharge chamber and is conducted to the outside towards the thermocouples via the steel with a thermal conductivity of 45 W/mK. A fraction of the heat entering the steel pole shoe may be dissipated to the sides into the magnets, which have a considerably lower thermal conductivity of 10 W/mK only. This configuration allows us to perform unperturbed temperature measurements on the outside of the pole shoe with insignificant thermal smearing.

Thermocouple voltages are recorded with two Pico Technology ADC24 devices. The cold junction is thermally insulated behind the thruster using multilayer insulation (MLI). PT-100 resistors near the pole shoe, radiator, and cold junction monitor temperatures, measured with a Pico Technology PT-104 device. Calibration was performed inside a heated shroud up to approximately 200°C, limited by wiring insulation. All temperature measurements were referenced to the PT-100 on the thruster housing inside the shroud.

Measurement error arises from voltage device accuracy and weld repeatability. Voltage measurement accuracy is 0.1%. Voltage variation among welds before calibration corresponds to about 2°C; after calibration against the PT-100, relative differences shrink to $\leq$ 0.1°C. Absolute temperature accuracy is less critical than relative differences, governed by PT-100 accuracy (3°C) and measurement device accuracy (0.015°C). Given the low relative uncertainty of the measured temperature after calibration, the system can precisely locate a gloved finger placed on the inside of the discharge chamber at ambient conditions. The relative uncertainty is thus omitted in the plots presented in Figs. 5 and 7.

Finally, a plasma diagnostic system mounted inside the test facility was used to spatially map the plume properties. This 5D gantry system moves the Faraday probe along three translational axes and two rotational axes (pitch and yaw), enabling 3D measurements. The current on the probe's collector surface is measured by a Keithley 2401 source meter. Details of the diagnostic system are described in Ref. [27]. Results are presented in Fig. 8.

The thruster is tested at different operating points covering mass flows of 0.3 to 0.5 mg/s xenon and applied anode voltages of 300 V to 700 V. These operating points have been previously characterized in Ref. [12], the test facility is described in Ref. [8, 13, 28]. The set points are controlled using a mass flow controller (MKS GE50A013501MBV020)

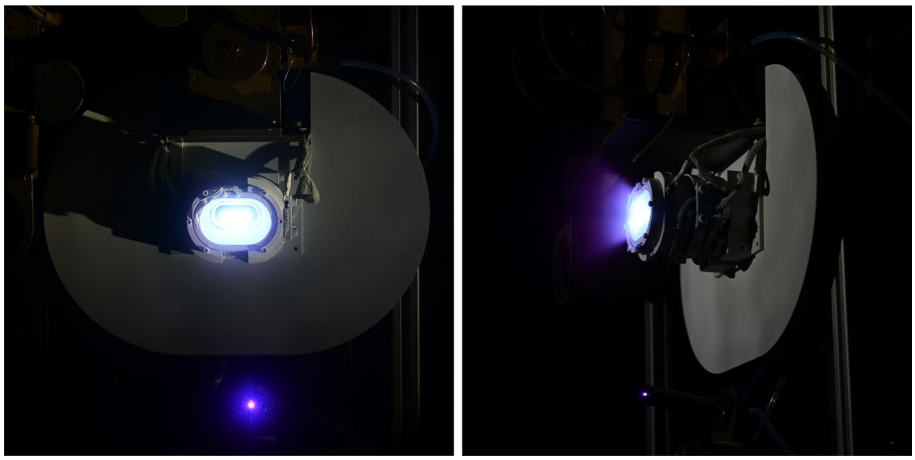


Fig. 3 Photographs of the linear ACFT in the Airbus Micro Newton test facility of the Laboratory for Enabling Technologies during the temperature testing. The harness, consisting primarily of shielded thermocouple wires, is visible, as is the hollow cathode below the thruster. The center region of the thruster is overexposed and shows the region of high electron density

and a FUG MCA 3000 3000 power supply. The pressure in the vacuum facility stayed below 2e-5 mbar nitrogen equivalent during thruster operation and was measured using a Pfeiffer PBR 260. The thrust is not measured since the additional measurement harness requires 50 electrical connections, which the thrust balance cannot provide. A total of 9 different operating points were tested, with steady-state thermal equilibrium only achieved at 4 power modes below 120 W, constrained by the maximum calibrated temperature of 200°C at the pole shoe. Figure 3 shows images of the thruster during testing. Detailed results are discussed in "Results" section.

Simulation

In previous works, full 3D plasma Particle-In-Cell (PIC) simulations were constrained by computational limitations, requiring coarse time steps between 10^{-9} and 10^{-11} seconds [19]. Spatial meshing was limited to a few hundred cells per dimension [20], or thruster models were scaled down by factors of 10 to 50 to reduce computation time [17]. While reducing time steps or mesh size is unavoidable when performing 3D simulations, resolving the full trajectory of a single electron, including its circumferential drift, requires simulating the entire discharge volume in 3D for up to 1 μs. Two-dimensional slices fail to capture the full 3D behavior. Although 2D simulations are suitable for studying other electron behaviors, they implicitly assume a uniform magnetic field along the circumference as well. Furthermore, using a 2D PIC simulation, [29] shows that differences in magnetic field strength between two CFTs can lead to variations in plasma behavior. Indicating that even local deviations, rather than just global differences between systems, can have a measurable impact.

Our simulation differs from previous studies by employing full 3D particle tracing rather than a PIC approach. Electron trajectories are computed under static electromagnetic fields, neglecting interactions with other electrons, ions, or neutral atoms, as well as any emergent effects from locally varying fields.

Depending on initial conditions, an electron typically requires between 10 and 1000 successful reflections at magnetic mirrors to complete one full circumferential orbit. While the simulation allows unlimited free paths truncated at 1 μs, the electron mean free path in an operating thruster depends on plasma and neutral gas densities and collision cross sections. Using typical xenon densities around 2×10^{20} m^{-3} [16] and relevant collision cross sections [30], electrons can traverse the discharge chamber 5 to 15 times before collisions, corresponding to drift lengths between approximately 0.01 and 1 times the thruster's circumference. This means that, while not all electrons will reach every region along the circumference in a real thruster, this drifting motion toward regions of inhomogeneous mirror strength can play a significant role.

The magnetic field inside the thruster is simulated using Ansys Maxwell based on detailed magnet geometries and magnetization properties. For a cylindrical ACFT, this produces a fully rotationally symmetric magnetic field; for the linear ACFT studied here, the symmetry reduces to a 180° rotational axis with two perpendicular mirror planes. Manufacturing imperfections further reduce this symmetry. A thorough mesh convergence study was performed to ensure simulation accuracy. The mesh surface deviation was progressively refined, focusing especially on the pole shoe surfaces where magnetic field gradients are steepest. Mesh refinements beyond a surface deviation of 0.01 mm did not significantly change the computed magnetic field values. Nevertheless, the mesh used for this analysis exhibits a surface deviation of 0.001 mm at the pole shoes and 0.01 mm at the anode and the magnets. The final mesh consists of approximately 2.8 million tetrahedrons, with a global solution error below 0.01%. Local errors near the pole shoe surfaces reach approximately 0.1% due to high field gradients. The simulation domain extends to ten times the thruster dimensions to avoid boundary artifacts. The resulting magnetic field is exported onto an equidistant grid with 0.1 mm spacing; further refinement was limited by computational resources but tests with coarser grids (0.25 mm) showed no qualitative differences in electron impact distributions.

The magnetic field grid is then imported into SIMION, where the electric field is set up and the particle tracing is performed using the static electric and magnetic fields. The discharge chamber walls and anode are assigned the full anode potential as boundary conditions, with a virtual grid at 80% of the anode potential in the exit plane representing the plasma sheath. This setup approximates the potential distribution found in full plasma simulations [16] while avoiding the computational cost of PIC methods. Here, the electron trajectories are governed by the Lorentz force without including particle-particle interactions or collisions. This approach is considered to be justified by the relatively long electron mean free path compared to the thruster dimensions.

Initial electron conditions are assigned using a Monte Carlo method based on PIC simulation data [16–18] and optical observations. Starting positions lie within 0 to 5 mm of the central plane between the racetrack's semi-circles, with initial velocity vectors angled up to 15° from this plane. Kinetic energies are uniformly distributed between 0 eV and the anode potential (300–700 eV). Sensitivity analyses show that electron impact distributions are robust to small variations in starting positions and angles of ± 2 mm and ± 10°. Simulations track 10^5 electron trajectories for up to 1 μs each on the full-sized thruster grid with 0.1 mm resolution. Time steps are adaptive and depend on

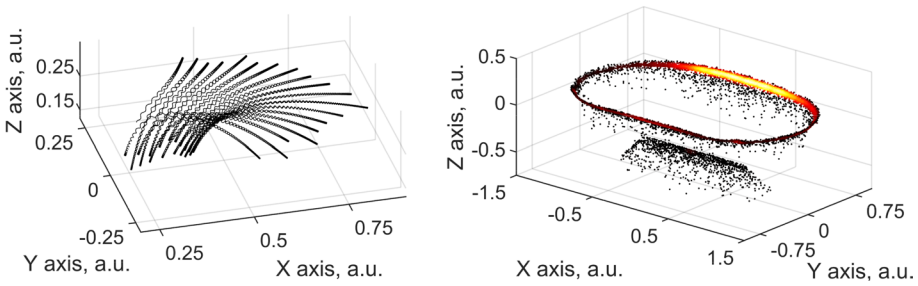


Fig. 4 Left: Trace of a single electron reflecting between anode (bottom) and pole shoe (side), gyrating about magnetic field lines and drifting circumferentially. Right: Normalized electron impact density on the discharge chamber inner surface, with highest impact regions near the pole shoe height and anode tip. Here, all points on the right represent the end point of a path as shown on the left

the velocity and the local gradient of the fields, but typically are around 10^{-13} seconds. Computation takes approximately 100 hours on an Intel(R) Core(TM) i7-6700 CPU.

Electrons gyrate around magnetic field lines, reflect between magnetic mirrors at cusps, and drift circumferentially due to combined electromagnetic forces. Those not meeting local mirror conditions eventually impact the discharge chamber walls near the pole shoes or anode. The simulated electron impact distributions are assumed to be related to temperature distribution. Figure 4 (left) shows a representative electron trajectory demonstrating gyration, reflection, and circumferential drift. The right panel presents a normalized map of electron impact density, highlighting high-loss regions near the pole shoe and anode tip. Every point on the right panel of Fig. 4 represents the end point of a path as shown in the left panel.

Additionally, these electron trajectories enable detailed analysis of out-of-plane drift phenomena. Similar to PIC results in Ref. [24], our particle tracing shows that near the thruster exit, the $E \times B$ drift dominates, accounting for about 99% of the drift velocity with typical values around 10^4 m/s. Near the center cusp and anode, where the electric potential gradient weakens, curvature and gradient drifts become significant, comprising over 50% of drift velocity with magnitudes between 10^2 and 10^3 m/s.

Results

The thruster operation procedure follows previously described works [12, 13]. Ignition of the hollow cathode neutralizer prior to thruster operation raises the overall temperature of the thruster and its thermocouples by a few degrees. However, since the cathode is not in direct line of sight of any thermocouples, temperature variations at those locations due to the cathode remain below 0.5°C. Once the thruster is firing, a temperature gradient develops around the pole shoe's circumference, which remains qualitatively consistent regardless of applied voltage, propellant flow rate, or firing duration. Thermocouples recording the highest steady state temperatures also show the earliest and steepest temperature rise immediately after ignition. This indicates localized heat deposition near these points, with conduction spreading heat throughout the pole shoe and establishing a gradient around its circumference. Looking at the steady state operation depicted in Figs. 5 and 7, the thermocouple which reaches 138°C, the highest temperature, has an initial increase of 1°C per 1 second while the coldest sensor initially

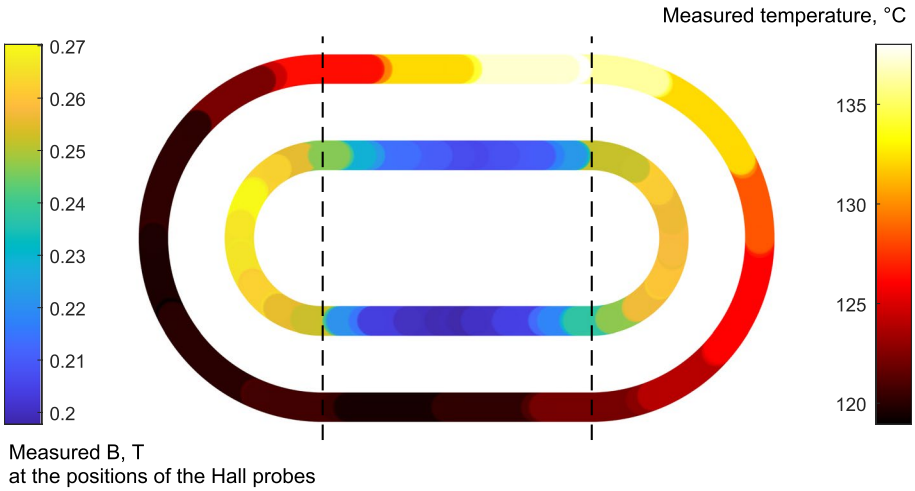


Fig. 5 Experimental measurements in the same coordinate system as Fig. 2: Two concentric ring-like color plots show spatial distributions along the racetrack circumference. **Inner ring**: Measured magnetic flux density (B-field) inside the non-operating thruster near the discharge chamber wall (approximately 2.5 mm from the pole shoe surface). The distribution deviates slightly from the expected symmetry, showing lower values at the linear sections and higher values near the semi-circular segments. **Outer ring**: Temperature distribution measured on the outside of the pole shoe during steady-state thruster operation at 700 V anode voltage, 0.3 mg/s Xe flow, and 74 mA ion current. A distinct hot spot appears at the top right segment, indicating localized heating

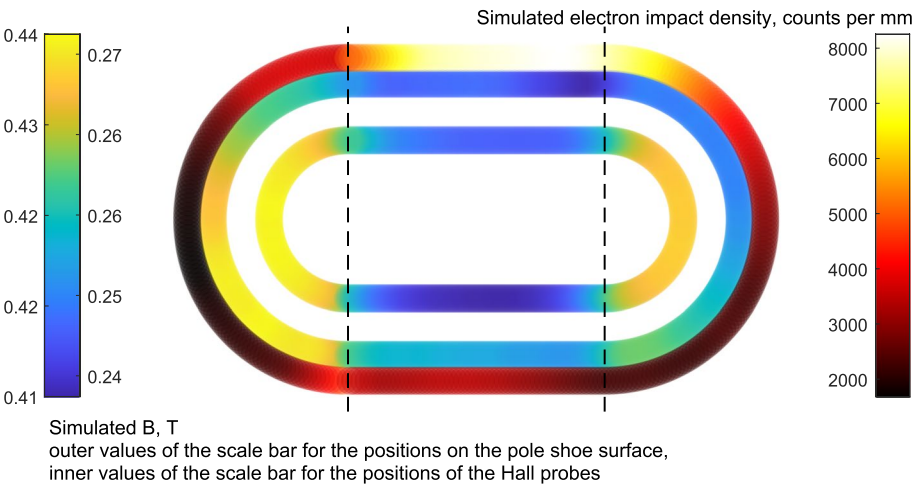


Fig. 6 Simulation results in the same coordinate system as Fig. 2: Three concentric ring-like color plots illustrate the simulated distributions along the pole shoe circumference. **Inner ring**: Simulated B-field magnitude at the Hall probe measurement locations, showing small variations and good agreement with experimental data in Fig. 5. **Middle ring**: Simulated B-field on the inner surface of the pole shoe, revealing stronger asymmetry with the weakest field (and thus weakest electron confinement) at the top right section. **Outer ring**: Simulated electron impact density on the discharge chamber wall, peaking at the same top right location, consistent with observed heating in the experiments

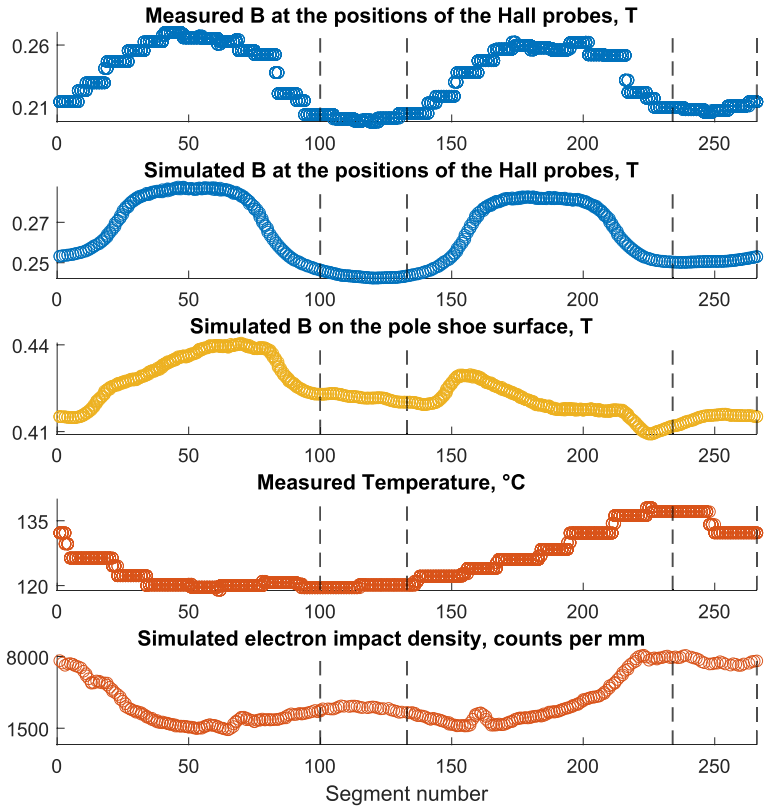


Fig. 7 Comparison of experimental and the simulated results as 2D plots with the same axis of abscissae given by a segmentation of the circumference. The dashed vertical lines indicate the contact points between semi-circular and linear sections of the circumference. Position 0 corresponds to the top left contact point, the position number increases anticlockwise. The top two plots show measured and simulated B-field in the region where the Hall probe can fit inside the thruster. The 3rd plot shows the simulated B-field on the inner surface of the pole shoe, where the magnetic mirror effect is strongest. The two plots at the bottom show the measured temperature on the outside of the pole shoe and the simulated electron impact density on its inner surface along the circumference

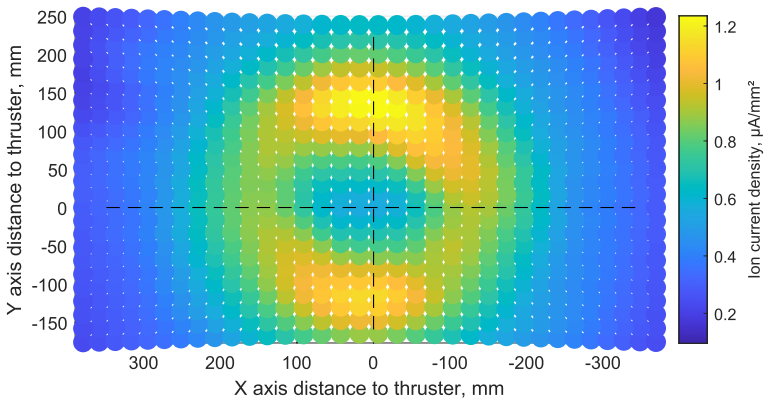


Fig. 8 2D color plot of the current density distribution in the X-Y plane at a distance of 200 mm from the thruster's exit plane. The data shows an asymmetry similar to the simulated electron impact distribution and the temperature distribution with a pronounced peak at the top and right and a secondary peak in the bottom left

increases at 1°C every 15 seconds and stabilizes at 119°C. At that operating point the outer housing of the thruster reached 71°C.

Figure 5 shows the measured absolute magnetic flux density approximately 2.5 mm from the pole shoe surface inside the non-operating thruster. Alongside, it presents the steady-state temperature profile on the pole shoe exterior during operation at 700 V anode voltage and 0.3 mg/s xenon flow, yielding a 74 mA ion current. The inner colored ring depicts the B-field distribution along the circumference, revealing lower values along the straight linear sections and higher values near the centers of the two semi-circular segments. Notably, the four contact points between the linear and curved sections, expected to be equivalent by symmetry, exhibit subtle but distinct differences, indicating weak asymmetries. The outer colored ring shows the temperature distribution along the outer pole shoe circumference. A pronounced hot spot appears in the top right corner, again contradicting the expected symmetry from the thruster's racetrack geometry.

We attribute the subtle B-field anomalies and the more pronounced temperature asymmetry to non-idealities in the magnetic configuration. Qualitatively identical temperature profiles were observed at all of the eight other operating points and during transient warm-up, confirming the reproducibility of this effect regardless of operating conditions.

To identify the most probable source of asymmetry, simulations were conducted varying the magnet properties within manufacturer tolerances. It was found that a 10° tilt of the second magnet's magnetization vector relative to the thruster's central axis best reproduces the measured B-field distribution. This tilt lies within typical fabrication variations [14, 15]. The direction of the component of the magnetization in the X-Y plane, i.e., perpendicular to the thruster's central axis, is indicated by (11) in Fig. 2. Figure 6 shows the corresponding simulated results: The simulated B-field at the locations of where the real probe locations were, closely match experimental data, while the B-field on the pole shoe surface exhibits a more pronounced asymmetry with a minimum at the top right of the circumference. The simulated electron impact density also peaks at this location, consistent with the hot spot observed in temperature measurements. The electron impacts presented in Fig. 6 are the same as in Fig. 4.

Figure 7 summarizes these findings by plotting measured and simulated values as functions of position along the pole shoe circumference. Although the total perimeter depends on the radii of the two semi-circles, each semi-circle is divided into 100 segments independent of radius. The linear sections are always divided into 30 segments each. Although this leads to non-uniform spacing along the circumference, it allows a better comparison between the correlated quantities at different distances from the surface of racetrack-like pole shoe. The dashed vertical lines in the figure represent the border between the semi-circular and linear sections (just like in Figs. 2, 5 and 6). Segment 0 corresponds to the contact point between top linear part and left semi-circle of the circumference (top left contact point), 100 to the bottom left, 130 to the bottom right, and 230 to the top right contact point. Segment 0 and segment 260 are equivalent. The segment number increases anticlockwise along the circumference.

Small yet significant deviations from perfect symmetry appear in the measured and simulated B-fields at the probe positions (top two plots). Here, the simulation is in good agreement with the measurements. At the pole shoe surface (third plot), the simulated

B-field asymmetry is more pronounced. The bottom two plots demonstrate a strong correlation between measured temperatures and simulated electron impact densities, both showing an asymmetry consistent with the magnetic field deviations. Where a weaker local B-field leads to more electrons reaching the walls, where their energy is lost and heats the pole shoe.

It is worth noting that, if the magnetic configuration is perfect, the resulting B-field distribution at the surface of the central pole shoe will exhibit the expected 180° symmetry. In this case, the B-field values along the circumference close to the pole shoe surface will vary between 0.42 T (middle of linear segments) to 0.43 T (center of the semi-circles). Comparing these ideal values to Fig. 6 shows that magnet misalignment reduces the minimum B-field and increases the maximum relative to the ideal case. The resulting electron impact distribution along the circumference also shows the expected symmetry with less fluctuations in the electron impact density, yielding a maximum of 6500 counts per mm only instead of more than 8000 counts per mm in the configuration of misaligned magnetization vectors between the first and second magnet. Furthermore, the average residence time of the electrons decreases by 10% to 20% once the misalignment of the magnetization vector of 10° is applied. Although it cannot be determined whether the enhanced electron impact density alone causes the observed temperature rise or if ion-wall interactions also contribute, a strong correlation exists between electron impact density and local temperature.

Finally, the influence of the magnetic configuration on the thruster plume profile was examined. The current-density profile measured by the 5D gantry equipped with a Faraday probe in the X-Y plane located 200 mm away from the thruster's exit plane is recorded at the chosen operating point of the thruster. The plasma diagnostic system is described in detail in Ref. [27]. The ion beam profile presented in Fig. 8 resembles a ring-shaped distribution similar to cylindrical ACFTs [27], but with significant asymmetries along the ring consistent with those seen in the electron impact and temperature profiles. The highest ion current density appears in the top right, with a secondary peak at the bottom left, and minima on the sides.

While this study does not include any plasma behavior, the observations suggest that magnetic field asymmetries influencing electron confinement also affect ion extraction and plume shape. This is in agreement with Ref. [21] and Ref. [22], where 2D PIC simulations show that the electron density in the center of the thruster can influence the plume. However, in this study, neither the particle tracing simulation nor the measurements of the temperature, the magnetic field inside the thruster or the ion density in the beam account for the plasma effects of a CFT, as these measurements regard unperturbed ions, electrons and electromagnetic fields. To gain further insights, in-situ plasma parameter measurements would be required to fully understand the link between the ion density distribution in the beam and the electron confinement inside the thruster.

Conclusion

This study combines experimental measurements and particle-tracing simulations to investigate the impact of magnetic field configuration on electron behavior and performance in a linear Advanced Cusp Field Thruster (ACFT). The linear ACFT's deliberate symmetry reduction, compared to the fully cylindrical variant, results in inherent spatial variations in the magnetic field along the racetrack-shaped pole shoe

circumference. These variations lead to localized differences in electron confinement efficiency due to spatially varying magnetic mirror strengths.

Simulations of ballistic electron trajectories, incorporating combined drifts from magnetic field gradients, curvature, and electric fields, reveal that electron residence time and impact distributions are sensitive to small deviations from ideal magnetic symmetry. These results predict non-uniform electron impact densities on the inner surface of the central pole shoe, with peaks coinciding with regions of reduced magnetic field strength.

Experimental measurements corroborate the simulation findings. Precise mapping of the magnetic flux density within the thruster matches simulations when manufacturing tolerances, specifically a 10° tilt in the second magnet's magnetization, are included. The measured temperature distribution on the outer pole shoe surface exhibits localized hot spots aligned with predicted regions of enhanced electron impacts, indicating that weaker local magnetic mirrors result in increased wall losses and heating. Moreover, asymmetries in the ion beam current density profile measured downstream of the thruster exhibit a similar result of these electron confinement variations. This suggests that variations of the B-field also influence overall thruster plume characteristics.

These findings imply that electron confinement in CFTs is effectively governed by the weakest points of the magnetic cusp structure around the circumference. Manufacturing and assembly tolerances, particularly magnet or magnetization misalignments, can significantly degrade confinement, causing localized heating and reducing efficiency. Although the linear sections of the thruster geometry feature inherently weaker magnetic gradients, the misalignment of the magnetization vector between the first and second magnet dominate the local mirror strength variations.

While our particle-tracing approach neglects plasma interactions, the strong correlation between simulations and experimental data supports the assumption of relatively long electron mean free paths within the discharge chamber. This suggests that ballistic electron dynamics primarily determine confinement quality. However, fully understanding the influence of localized confinement weaknesses on overall thruster performance, including plasma behavior and ion wall interactions, requires further investigation.

In conclusion, this work demonstrates that even minor deviations from ideal magnetic configurations significantly impact electron confinement and thruster behavior in linear ACFTs. Our integrated experimental and simulation approach provides a predictive framework to assess magnetic non-idealities, guiding design improvements and quality assurance in CFT development. Future studies incorporating full 3D plasma modeling and in-situ plasma parameter measurements will be essential to understand the complex coupling between electron dynamics, plasma behavior, plume distribution and overall thruster performance.

Acknowledgements
This project has received funding from the European Union's Horizon 2020 research and innovation program under grant agreement No. 870336. The authors would like to thank the participating team at Airbus Friedrichshafen.

Authors' contributions
L.B. wrote the main manuscript. L.B. conducted the experiments, analysis and prepared the figures. All authors reviewed the manuscript and provided feedback.

Funding
Open Access funding enabled and organized by Projekt DEAL.

Data availability
Measurement data for the B-field, the Temperature and the plasma plume Simulation data for the electron impacts and the magnetic field in the relevant region https://doi.org/10.22029/jlupub-19648.

Declarations

Competing interests
The authors declare no competing interests.

Received: 28 February 2025 Accepted: 11 July 2025
Published: 4 August 2025

References

1. Holste K, Dietz P, Scharmann S et al (2020) Ion thrusters for electric propulsion: scientific issues developing a niche technology into a game changer. Rev Sci Instrum 91(6):061101
2. Goebel DM, Katz I (2008) Fundamentals of Electric Propulsion. John Wiley & Sons Inc, Hoboken. https://doi.org/10.1002/9780470436448
3. Zhurin V et al (1999) Physics of closed drift thrusters. Plasma Sources Sci Technol 8:R1. https://doi.org/10.1088/0963-0252/8/1/021
4. Kornfeld G, Koch N, Coustou G (2003) The Highly Efficient Multistage Plasma (HEMP) thruster, a new electric propulsion concept derived from tube technology. In 4th IEEE International Conference on Vacuum Electronics, 2003, 3–4. https://doi.org/10.1109/ivec.2003.1285973
5. Courtney D, Martinez-Sanchez M (2007) Diverging Cusped-Field Hall Thruster (DCHT) IEPC-2007-39. In: 30th International Electric Propulsion Conference. Electric Rocket Propulsion Society. https://api.semanticscholar.org/CorpusID:115148534
6. Janes G, Wilson T (1962) Electrostatic acceleration of neutral plasmas - momentum transfer through magnetic fields. In: Proceedings of the Third Symposium on Advanced Propulsion. Avco Corp. Avco-Everett Research Lab., Everett, Mass; United States. https://www.osti.gov/biblio/4769285
7. Keller A, Köhler P, Hey F, et al (2013) Parametric Study of HEMP-Thruster Downscaling to ${\mu} $ N Thrust Levels. IEEE Transactions on Plasma Science. Electric Rocket Propulsion Society 43(1)45–53. https://doi.org/10.1109/TPS.2014.2321095
8. Hey FG (2018) Micro Newton Thruster Development. Springer Vieweg. Hey Franz Georg. Micro Newton Thruster Development. https://doi.org/10.1007/978-3-658-21209-4
9. Vaupel M, Hey FG, et al (2015) The Next Generation milli-Newton µHEMPT as potential main Thruster for small satellites. In Proceedings of the 35th International Electric Propulsion Conference (IEPC).
10. Vaupel M, Kottke N, et al (2021) Development status of the Advanced Cusp Field Thruster propulsion system. Paris, France
11. Vaupel M, Kottke NG, et al (2022) iodine Fed Advanced Cusp Field Thruster Endurance Test Results. In: 8th Edition of the Space Propulsion Conference. Paris, France
12. Bauer L, Vaupel M, et al (2022) Advanced Cusp Field Thruster upscaling with Alternative Scaling Schemes. In: 8th Edition of the Space Propulsion Conference. Paris, France
13. Blättermann H, et al (2024) Endurance testing and characterization of a novel candidate for CubeSat propulsion: The Advanced Cusp Field Thruster (ACFT). Acta Astronautica 219;906–916. issn:0094-5765. https://doi.org/10.1016/j.actaastro.2024.03.074. https://www.sciencedirect.com/science/article/pii/S0094576524001991
14. Hilzinger R, Rodewald W (2012) Magnetic materials. Publicis MCD Verlag
15. Börgermann FJ, Blank R, Reppel G, et al (2008) Improved homogenity of permanent magnets for undulators and wigglers. EPAC08.
16. Brandt T, et al (2016) Particle-in-Cell Simulation of a Down-Scaled HEMP Thruster. JSASS Aerospace Tech Japan
17. Kalentev O, Matyash K, Duras J et al (2014) Electrostatic Ion Thrusters - Towards Predictive Modeling. Contrib Plasma Phys 54(2):235–248. https://doi.org/10.1002/ctpp.201300038
18. Matyash K, Schneider R et al (2010) Kinetic Simulations of SPT and HEMP Thrusters Including the Near-Field Plume Region. IEEE Trans Plasma Sci 38(9):2274–2280. https://doi.org/10.1109/tps.2010.2056936
19. Fabris A, Young C, et al (2013) Ion Velocimetry Measurements and Particle-In-Cell Simulation of a Cylindrical Cusped Plasma Accelerator. IEEE Trans Plasma Sci 43:54–63. https://doi.org/10.1109/TPS.2014.2321743
20. Matyash K, et al (2009) Kinetic simulation of the stationary HEMP thruster including the near–field plume region. In: The 31rd International Electric Propulsion Conference: Electric Rocket Propulsion Society
21. Duras J, Schneider R, et al (2016) Influence of Electron Sources on the Near-field Plume in a Multistage Plasma Thruster. Plasma Phys Technol J 3:126–130. https://doi.org/10.14311/ppt.2016.3.126
22. Duras J, Kahnfeld, et al (2017) Ion angular distribution simulation of the highly efficient multistage plasma thruster. J Plasma Phys 83(1). https://doi.org/10.1017/S0022377817000125
23. Chen FF (2015) Introduction to plasma physics and controlled (Vol. 1, pp. 19-51). New York: Plenum press.
24. Liu H, Wu H et al (2014) Study of the electric field formation in a multi-cusped magnetic field. Phys Plasmas 21. https://doi.org/10.1063/1.4896250https://doi.org/10.1063/1.4896250
25. Lewerentz L et al (2022) Pic simulations of the ms4 thruster. Front Phys 10–2022. https://doi.org/10.3389/fphy.2022.833159
26. Vaupel M, et al (2018) Performance of the mN-HEMPT with iodine and xenon. In: 6th Edition of the Space Propulsion Conference
27. Bauer L, Vaupel M, Blättermann H, et al (2026) Direct comparison of different probe positioning and pointing schemes for plume measurements using an Advanced Cusp Field Thruster. J Electr Propuls 5(10).https://doi.org/10.1007/s44205-026-00182-0

28. Hey VM F G, et al (2019) Inter-Laboratory Comparison: Tests of a single thruster in two different facilities, on two different thrust balances. In: The 36rd International Electric Propulsion ConferencePublisher: Publisher: Electric Rocket Propulsion Society
29. Zhao YJ et al (2013) Particle-in-cell simulations for the effect of magnetic field strength on a cusped field thruster. J Phys D Appl Phys 47(4):045201. https://doi.org/10.1088/0022-3727/47/4/045201
30. Perkins ST, Cullen DE, Seltzer SM (1991) Tables and graphs of electron-interaction cross sections from 10 eV to 100 GeV derived from the LLNL Evaluated Electron Data Library (EEDL), Z = 1–100. UCRL-50400, 31, 21-24.

Publisher's Note

Springer Nature remains neutral with regard to jurisdictional claims in published maps and institutional affiliations.